

pubs.acs.org/JPCL Letter

# Three-Dimensional Fully Conjugated Covalent Organic Frameworks for Efficient Photocatalytic Water Splitting

Yangyang Wan,\* Pengting Sun, Lebin Shi, Xiaohong Yan, and Xu Zhang\*



Cite This: J. Phys. Chem. Lett. 2023, 14, 7411-7420



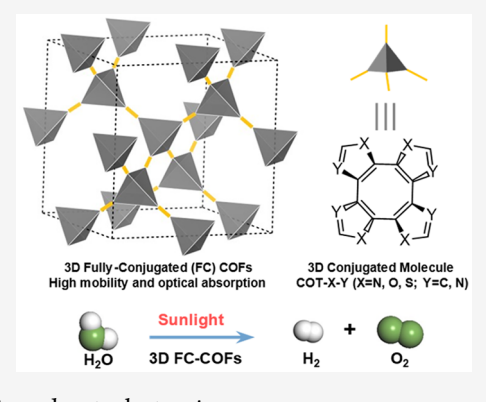
**ACCESS** 

III Metrics & More

Article Recommendations

s Supporting Information

ABSTRACT: Covalent organic frameworks (COFs) are promising photocatalysts for water splitting, but their efficiency lags behind that of inorganic counterparts partly due to the limited charge transport and optical absorption properties. To overcome this limitation, we proposed to employ three-dimensional (3D) fully conjugated (FC) COFs with a topological assembly of cyclooctatetraene derivatives for photocatalytic water splitting. On the basis of first-principles calculations, we demonstrated that these 3D FC-COFs are semiconductors with exceptional charge transport and optical absorption properties. The carrier mobilities are comparable to those of inorganic semiconductors and superior to the record mobility observed in two-dimensional COFs. Additionally, the 3D FC-COFs exhibit broad visible light absorption with direct band gaps and high optical absorption coefficients. Among them, two 3D FC-COFs are identified for overall water splitting, while three others can facilitate the hydrogen evolution half-reaction. This study pioneers the design of



3D FC-COF photocatalysts, potentially advancing their applications in photocatalysis and optoelectronics.

Photocatalytic water splitting for hydrogen production is a highly appealing technology for sustainable and environmentally friendly energy sources. 1-4 Recently, covalent organic frameworks (COFs) have emerged as a promising class of photocatalysts for water splitting, owing to their unique structural and physicochemical properties. 5-12 In particular, COFs can be designed using a bottom-up approach, and their rich molecular building blocks provide versatile properties such as a large surface area, abundant active sites, and high crystallinity and stability, making them ideal candidates for water splitting are based on two-dimensional (2D) conjugated structures, 6,12-20 with very few based on three-dimensional (3D) non-fully conjugated structures. It has been reported that the hydrogen production rate exceeds 40 mmol g<sup>-1</sup> h<sup>-1</sup> for a few of the COF photocatalysts. 23,24

However, despite the promising results obtained thus far, the solar-to-hydrogen and/or quantum efficiency of COF photocatalysts for water splitting still lags behind those of other wellestablished photocatalytic materials, particularly inorganic ones. This is partly due to the structural characteristics of 2D COFs and 3D non-fully conjugated COFs imposing limitations on the complete delocalization and transportation of charge carriers. More specifically, conjugated orbitals form within the plane in 2D COFs, while weak van der Waals interactions ( $\pi$ – $\pi$  stacking) form in the direction perpendicular to the plane, resulting in the slow interplane transition of charge carriers. Similarly, in 3D non-fully conjugated structures, the extension of the conjugation across the 3D skeleton is interrupted due to the inclusion of sp³ carbon-based

tetrahedral building blocks.  $^{25,26}$  The reported values of carrier mobility in 2D COFs typically fall within the range of 0.1-20 cm $^2$  s $^{-1}$  V $^{-1}$  for both electrons and holes,  $^{27-29}$  which are significantly lower than those observed in inorganic materials.  $^{30,31}$  Although various strategies for enhancing the mobility of 2D COFs through structural and component engineering exist, the inherent non-fully conjugated nature hampers further improvements in the photocatalytic performance of these COF photocatalysts.

In recent years, a new type of COF called 3D fully conjugated COFs (FC-COFs) has emerged as a promising class of materials for applications. These FC-COFs are synthesized using cyclooctatetraene (COT) and its derivatives as building blocks with a saddle-shaped 3D architecture.  $^{26,32-35}$  Unlike the 2D and 3D non-fully conjugated COFs, these materials possess a fully conjugated structure in a three-dimensional framework, with all building blocks connected by alternating single and double bonds and delocalized  $\pi$ -electrons extending in all three dimensions. This unique structure gives rise to exceptional electronic and optical properties, including high carrier mobility and broad light absorption. As a result, FC-COFs hold great potential to

Received: July 5, 2023 Accepted: August 10, 2023 Published: August 14, 2023





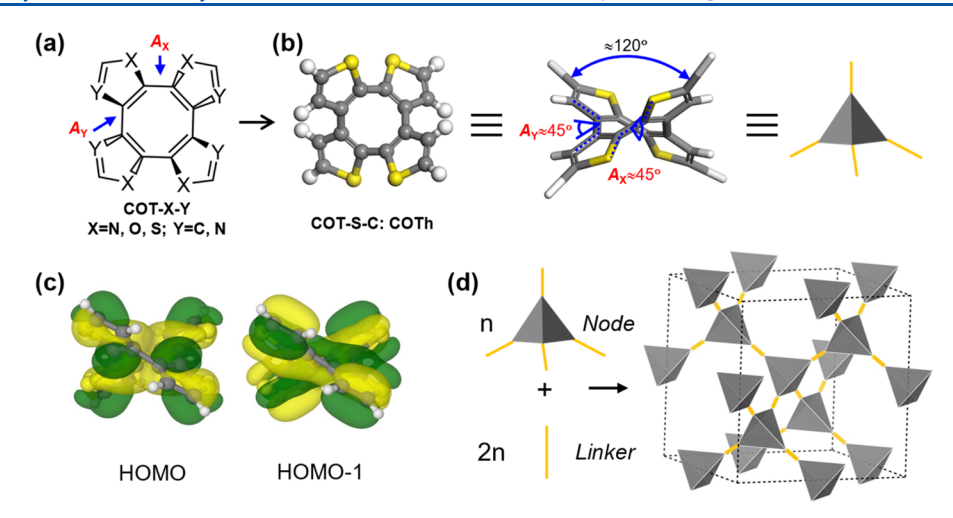


Figure 1. (a) Chemical structures of heteroarene-fused COT derivatives (COT-X-Y, where X = N, O, or S and Y = C or N). The dihedral angles between adjacent thiophene molecules are represented by  $A_X$  (X-C-C-X dihedral angle) and  $A_Y$  (Y-C-C-Y dihedral angle). (b) Schematic structures of the cyclooctatetrathiophene (COTh, COT-S-C) molecule. The gray, yellow, and white spheres represent carbon, sulfur, and hydrogen atoms, respectively. (c) Highest occupied molecular orbital (HOMO) and first orbital below the HOMO (HOMO-1) of COTh. (d) Schematic diagram of building a 3D FC-COF from a COT molecule (*Node*).

overcome the challenges that the 2D and 3D non-fully conjugated COFs meet in photocatalytic water splitting and optoelectronics. However, the current understanding of the structural and optoelectronic properties of FC-COFs is still limited. In particular, the possibility that the FC-COFs yield efficient photocatalytic water splitting is unknown. Answers to these fascinating questions could have substantial impacts on the applications of 3D FC-COFs in the fields of photocatalysis and optoelectronics.

In this study, we proposed six 3D FC-COFs with a topological assembly of COT derivatives (COF-COT-X-Y, where X = N, O, or S and Y = C or N) and strived to establish the structure-property relationship in these 3D FC-COFs for photocatalytic water splitting by performing first-principles calculations. We focus on transportation of photogenerated carriers and optical absorption, which are critical factors that determine the solar-to-hydrogen efficiency in COF photocatalysts.<sup>36</sup> It is demonstrated that these 3D FC-COFs are semiconductors with desirable carrier transport and optical absorption properties. The materials exhibit tunable direct band gaps ranging from 1.75 to 2.68 eV and high optical absorption coefficients exceeding  $2 \times 10^5$  cm<sup>-1</sup> in the visible light range. In addition, the 3D FC-COFs have a quasiisotropic character of carrier transport, with mobilities reaching 480 and 1400 cm<sup>2</sup> s<sup>-1</sup> V<sup>-1</sup> for the hole and electron, respectively. These values are comparable to those of inorganic semiconductors (e.g., SiC,<sup>30</sup> 400–900 cm<sup>2</sup> s<sup>-1</sup> V<sup>-1</sup> for the electron; CsPbI3,<sup>37</sup> 1399 cm<sup>2</sup> s<sup>-1</sup> V<sup>-1</sup> for the electron and 140 cm<sup>2</sup> s<sup>-1</sup> V<sup>-1</sup> for the hole; GaAs,<sup>31</sup> 3000 cm<sup>2</sup> s<sup>-1</sup> V<sup>-1</sup> for the electron) and T-carbon<sup>38</sup> (2360 cm<sup>2</sup> s<sup>-1</sup> V<sup>-1</sup> for the electron and  $270 \text{ cm}^2 \text{ s}^{-1} \text{ V}^{-1}$  for the hole) and superior to the recorded mobility of 2D COFs (165 cm<sup>2</sup> s<sup>-1</sup> V<sup>-1</sup>).<sup>39</sup> Notably, two of the 3D FC-COFs have demonstrated potential as overall water splitting photocatalysts, while three others can be used as photocatalysts for hydrogen evolution half-reactions. This study is an attempt to design 3D FC-COFs as photocatalysts for water splitting and could accelerate photocatalytic and optoelectronic applications of 3D FC-COFs.

The 3D FC-COFs were constructed using fragments based on heteroarene-fused COT derivatives, as shown in Figure 1a.

These molecules have inherently nonplanar, saddle-shaped configurations and are experimentally feasible. 26,40 The molecules can be modified with heteroatoms on the X and Y sites and are denoted as COT-X-Y (where X = N, O, or S and Y = C or N) in the following. The dihedral angles between adjacent thiophene molecules are represented by A<sub>X</sub> (X-C-C-X dihedral angle) and  $A_v$  (Y-C-C-Y dihedral angle). Using COF-S-C as an example, whose chemical structure is shown in Figure 1b, the fragment results in the cyclooctatetrathiophene (COTh) molecule. The  $A_X$  and  $A_Y$  values in COTh are approximately 45°, and the dihedral angle between para thiophene molecules is ~120°, making it approximately a tetrahedral building block. Figure 1c displays the highest occupied molecular orbital (HOMO) and the first orbital below the HOMO (HOMO−1) of COTh. The orbitals are distributed throughout the entire molecular structure with significant overlap, indicating a strong  $\pi$ -conjugation nature within the 3D saddle-shaped configuration. FC-COFs based on COT molecules can be synthesized through two conceptual steps: (1) the synthesis of COT molecules and (2) the coupling of these COT molecules to form FC-COFs.<sup>26</sup> In the latter step, a linear molecule with  $C_2$  symmetry is commonly employed as the linker for the coupling of COT molecules, <sup>26,33</sup> as depicted in Figure 1d. The orthotetrahedrally shaped node and linear linker result in a 3D FC-COF with a diamond-like structure, similar to previously reported T-carbon.<sup>41</sup> In this work, to simplify the theoretical model and save computational costs, the 3D FC-COFs are constructed by directly linking with COT building blocks, namely, without linear molecular linkers. As this method is experimentally feasible and represents the smallest 3D FC-COFs based on COT building blocks, the general trends observed in this work could be extrapolated to other 3D FC-COFs. Six 3D FC-COFs were investigated with various combinations of X and Y atoms on COT and are denoted as COF-COT-X-Y (where X = N, O, or S and Y = Cor N) in the following.

The structural stability of the COFs is verified with the calculated phonon spectrum and first-principles molecular dynamics (MD) simulations. As shown in Figure S1, the phonon spectrum does not reveal any imaginary vibration

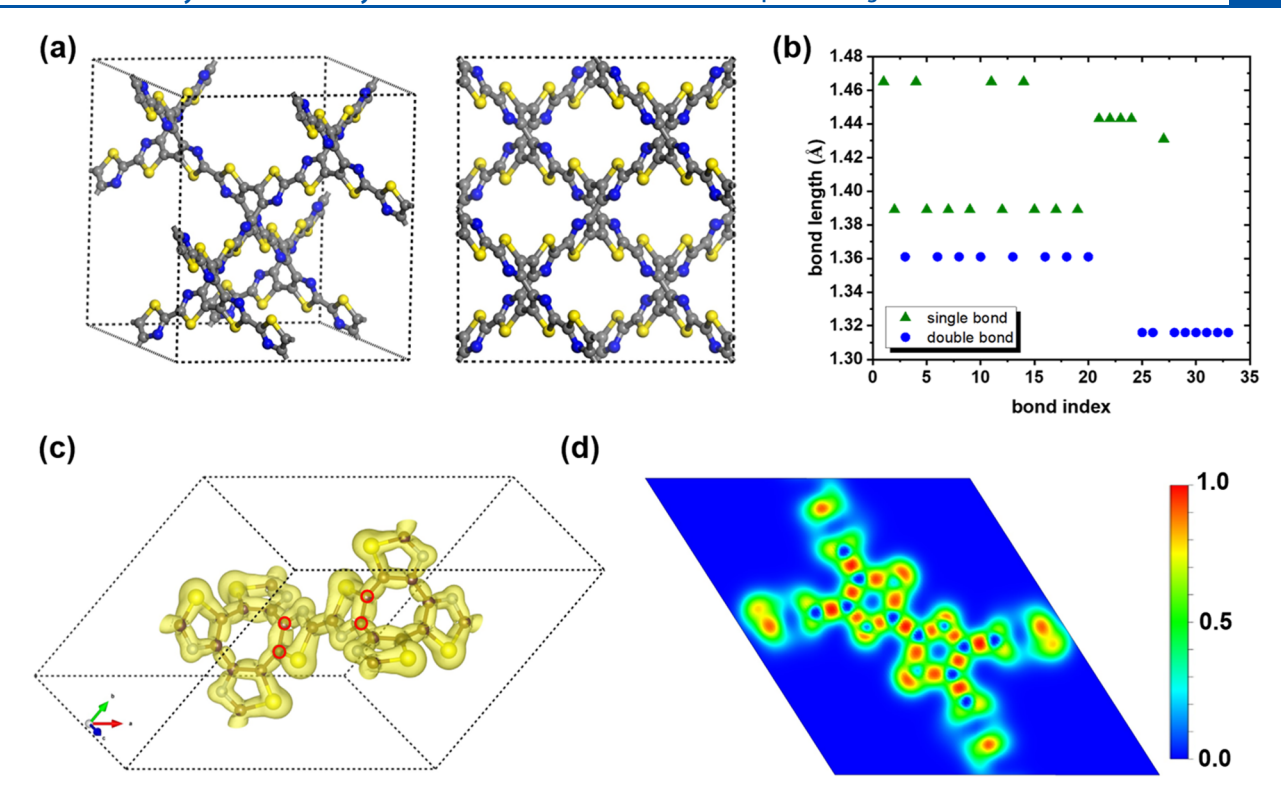


Figure 2. (a) Optimized structure of COF-COT-S-N with a side view. Gray, yellow, and blue spheres represent carbon, sulfur, and nitrogen atoms, respectively. (b) Double and single bond lengths in COF-COT-S-N. (c) Largely overlooked localized orbital locator (LOL) with an isosurface of 0.5. (d) Two-dimensional display of LOL, where the plane intersects the carbon atoms labeled with the red circles in panel c.

Table 1. Summary of Lattice Constants (a, b, and c in angstroms) and Angles  $(\alpha, \beta, \text{ and } \gamma \text{ in degrees})$ , Cell Volumes (V in cubic angstroms), Diameters of the Largest Included Sphere (LSD in angstroms), Dihedral Angles  $(A_X \text{ and } A_Y \text{ in degrees})$ , Average Double and Single Bond Lengths  $(L_{\text{DB}} \text{ and } L_{\text{SB}} \text{ in angstroms})$ , and Differences between  $L_{\text{DB}}$  and  $L_{\text{SB}} (\Delta L)$ 

COF-COT-	а	ь	с	α, β, γ	V	LSD	$A_{\mathrm{X}}$	$A_{ m Y}$	$L_{ m DB}$	$L_{ m SB}$	$\Delta L$
N-C	23.83	21.85	16.02	90	8344	10.5	43.82	42.97	1.392	1.430	0.038
O-C	22.04	21.30	17.19	90	8069	11.3	50.16	50.24	1.375	1.428	0.053
S-C	24.52	20.87	17.74	90	9078	11.7	45.76	42.59	1.387	1.435	0.048
N-N	21.89	21.63	15.93	90	7542	10.8	48.44	48.60	1.349	1.416	0.067
O-N	21.29	21.44	15.69	90	7161	9.9	42.16	42.60	1.341	1.408	0.067
S-N	24.87	19.68	16.62	90	8134	10.6	45.93	44.56	1.339	1.423	0.084

modes, indicating the lattice stability of the COFs. MD simulations were conducted at a temperature of 300 K by using the NVT ensemble. Figure S1 illustrates the structural snapshots taken at 6 ps during the MD simulations. It is apparent that the COFs maintain their lattice structures without any cleavage of chemical bonds or formation of new chemical bonds, thus confirming their structural stability at room temperature. Figure 2a depicts the optimized structure of COF-COT-S-N with a side view. Due to the imperfect orthotetrahedral shape of the COT-S-N molecule, the symmetry of the optimized COF is reduced to FDDD (space group 70). Other 3D FC-COFs exhibit similar structures and the same space group as those of COF-COT-S-N, with their detailed structural information presented in Table 1. Generally, COFs with larger atomic radius combinations of X and Y atoms exhibit larger lattice constants (a, b, and c), cell volumes (V), and diameters of the largest included sphere (LSD). For instance, in COF-COT-X-C (X = N, O, or S) systems with carbon atoms at site Y, both V and LSD increase as X atoms change from O to N and S. Similarly, in COF-COT-S-Y (Y = C or N) systems with sulfur atoms at site X, both V and LSD

increase as Y atoms change from N to C. As a result, COF-COT-S-C has the largest V of 9078 Å<sup>3</sup> and the largest LSD of 11.7 Å. In addition, a slight change in the dihedral angle ( $A_{\rm X}$  and  $A_{\rm Y}$ ) relative to the isolated COT molecule ( $A_{\rm X}$  and  $A_{\rm Y} \approx 45^{\circ}$ ) is observed on the COT building blocks of 3D FC-COFs, as summarized in Table 1.

In conjugated systems, the  $\pi$ -electrons are delocalized over the entire system, resulting in a longer double bond length and a shorter single bond length than those of isolated double and single bonds, respectively. Therefore, we analyzed the bond lengths of single and double bonds in 3D FC-COFs. With COF-COT-S-N as an example, as illustrated in Figure 2b, the single and double bond lengths vary from 1.389 to 1.465 Å and from 1.316 to 1.361 Å, respectively. The detailed bond lengths and bond indices of COF-COT-S-N can be found in Figure S2. The average double and single bond lengths ( $L_{\rm DB}$  and  $L_{\rm SB}$ , respectively) in COF-COT-S-N are determined to be 1.339 and 1.423 Å, respectively. The  $L_{\rm DB}$  is larger than that of the double bond in ethylene (1.332 Å), while the  $L_{\rm SB}$  is shorter than that of the single bond in ethane (1.470 Å), suggesting a conjugated nature in COF-COT-S-N. Similar trends are

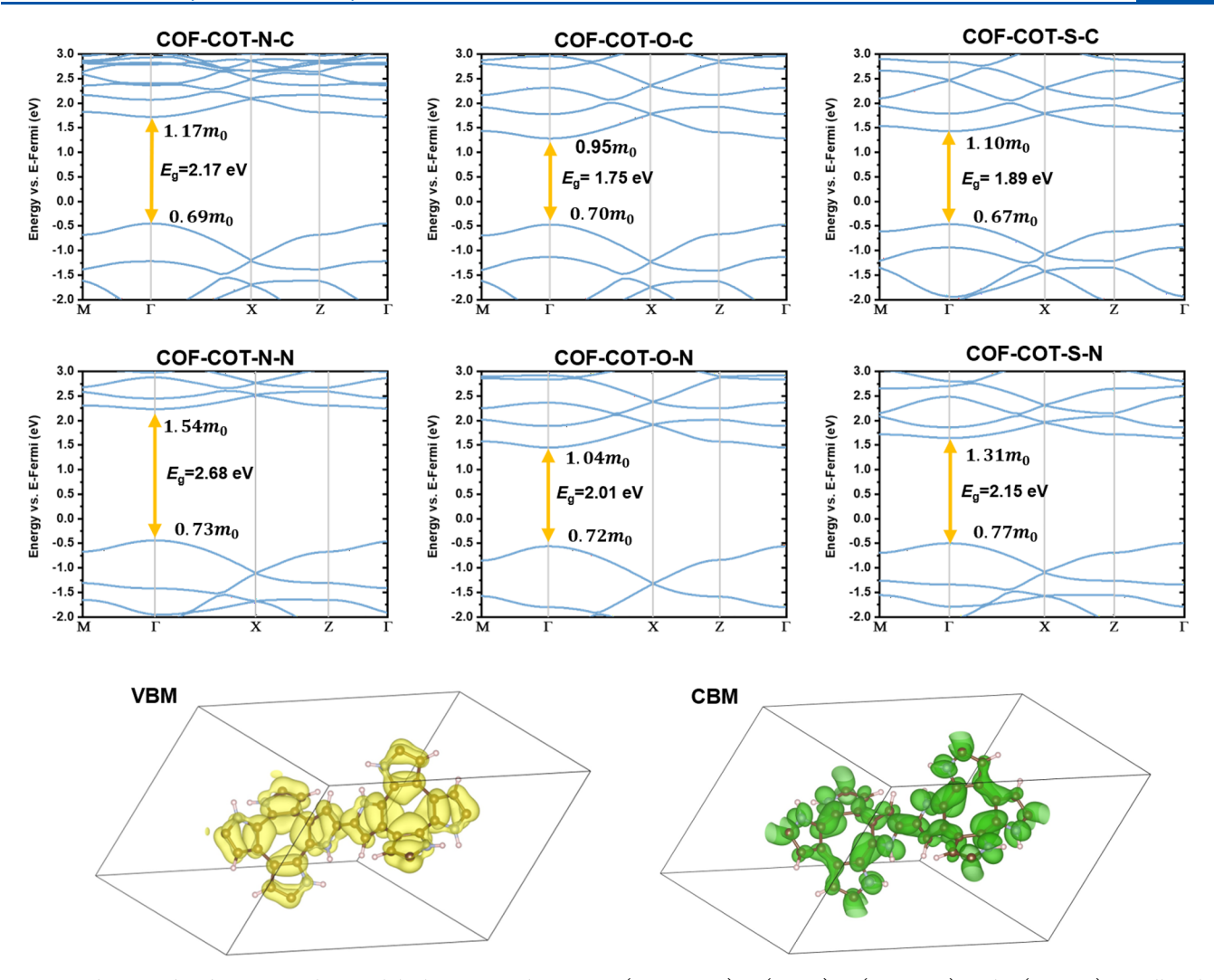


Figure 3. Electronic band structures along with high-symmetry k-points M (0.5, 0.5, 0.5),  $\Gamma$  (0, 0, 0), X (0, 0.5, 0.5), and Z (0, 0, 0.5) as well as the partial charge densities of the valence band maximum (VBM) and conduction band minimum (CBM) in COF-COT-N-C. All COFs have direct band gaps ( $E_g$ ) represented by the yellow arrows. The effective mass ( $m^*/m_0$ ) from  $\Gamma$  to X of the hole and electron is also displayed.

Table 2. Summary of Effective Masses  $(m^*/m_0)$  for Electrons and Holes in the  $\Gamma$  to X Direction, Deformation Potential Constants  $(E_1)$ , 3D Elastic Constants  $(C_{3D})$ , and Carrier Mobilities  $(\mu)$  at 300 K

				$\mu \text{ (cm}^2 \text{ s}^{-1} \text{ V}^{-1})$		
COF-COT-	$m^*/m_0$ (hole/electron)	$E_1$ (eV) (hole/electron)	$C_{\rm 3D}~(10^9~{\rm N~m^{-2}})$	hole	electron	
N-C	0.69/1.17	-7.21/-2.43	94.2	282.5	663.2	
O-C	0.70/0.95	-5.89/-2.34	110.9	480.5	1418.3	
S-C	0.72/1.10	-6.79/-2.84	79.7	242.6	479.8	
N-N	0.73/1.54	-7.70/-2.97	106.3	243.1	252.8	
O-N	0.72/1.04	-5.89/-2.74	104.7	422.9	779.0	
S-N	0.77/1.31	-9.75/-5.88	86.7	107.9	78.8	

observed in other 3D FC-COFs, as summarized in Table 1 and Figure S3.  $L_{\rm SB}$  and  $L_{\rm DB}$  range from 1.408 to 1.435 Å and from 1.339 to 1.392 Å, respectively. The difference between  $L_{\rm SB}$  and  $L_{\rm DB}$  ( $\Delta L$ ) ranges from 0.038 to 0.084 Å, which is smaller than the bond difference (0.138 Å) between the single bond in ethane (1.470 Å) and the double bond in ethylene (1.332 Å), suggesting the fully conjugated nature of the 3D FC-COFs' backbones. The fully conjugated nature can also be represented by the largely overlooked localized orbital locator (LOL). As shown in Figure 2c for COF-COT-S-N, the LOL with an isosurface of 0.5, which typically represents a uniform

electron gas, spreads throughout the entire 3D framework. The 2D display of LOL also confirms the fully conjugated nature, as depicted in Figure 2d.

The electronic and optical properties of 3D FC-COFs could benefit from their fully conjugated nature, such as a high carrier mobility and broad light absorption. To investigate their optoelectronic properties, we calculated the electronic band structures using the HSE06 method at first. Figure 3 illustrates the band structures along high-symmetry k-points from M (0.5, 0.5, 0.5),  $\Gamma(0, 0, 0)$ , and X(0, 0.5, 0.5) to Z(0, 0, 0.5). All COFs have direct band gaps  $(E_{\sigma})$  at the  $\Gamma$  k-point, ranging

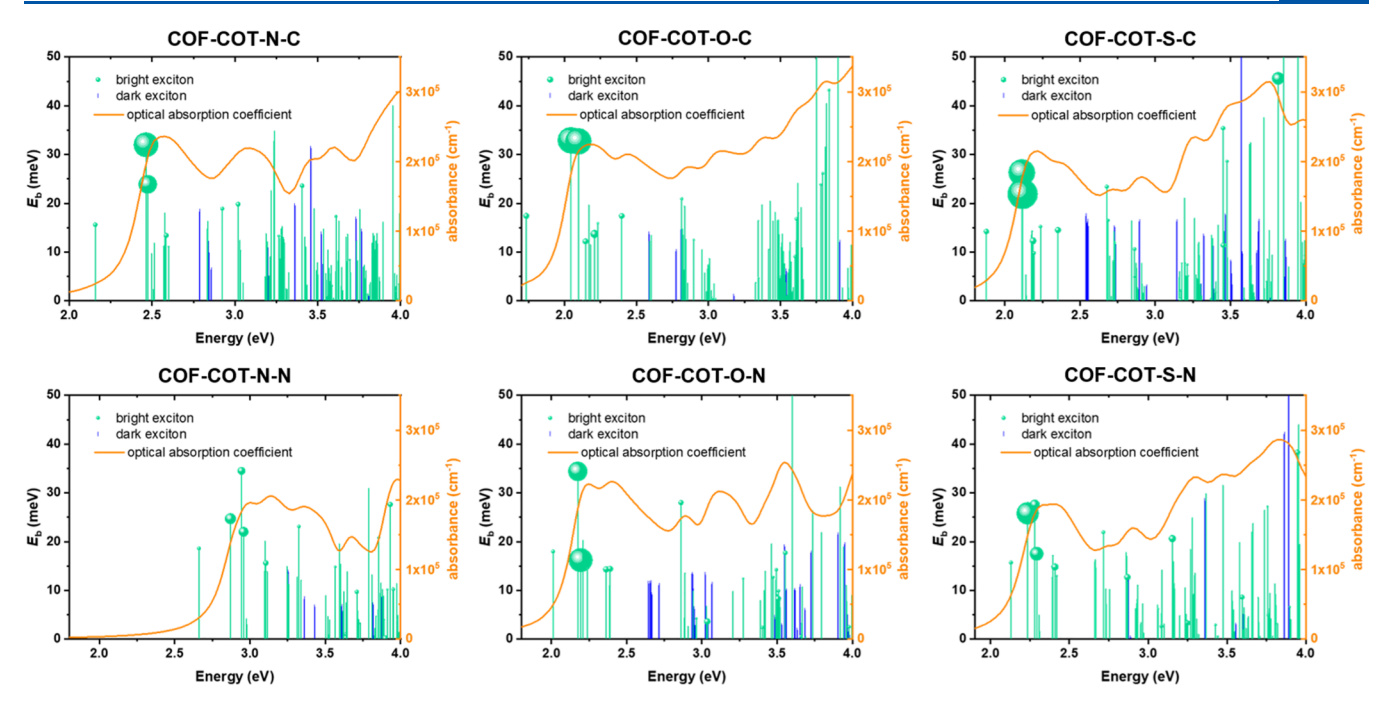


Figure 4. Optical absorption coefficients and exciton binding energies  $(E_b)$  of the low-energy (<4.0 eV) excitons of 3D FC-COFs calculated with TDDFT on top of HSE06. The oscillator strength of the bright excitons is represented by green spheres, with larger spheres indicating higher oscillator strengths.

from 1.75 to 2.68 eV, indicating the rich tunability of electronic properties and broad optical absorption in the 3D FC-COFs. The valence band maximum (VBM) and conduction band minimum (CBM) of COF-COT-N-C are illustrated with the partial charge density at the  $\Gamma$  k-point, as shown in the bottom panels of Figure 3. The VBM and CBM are delocalized throughout the whole 3D framework, consistent with the conjugated nature, and the dispersive valence and conduction bands also support this characteristic, suggesting good transport properties in the 3D FC-COFs.

Then, we calculated the carrier mobility in these 3D FC-COFs using the deformation potential theory proposed by Bardeen and Shockley (see the computational details in Methods). As shown in eq 1, the effective mass  $(m^*)$  plays a crucial role in determining the carrier mobility. The effective masses along the  $\Gamma$  to M,  $\Gamma$  to X, and  $\Gamma$  to Z directions are summarized in Table S1 and Table 2. On the basis of the effective mass values along the three directions, it was found that the 3D FC-COFs exhibit a quasi-isotropic transport character. The effective mass of holes is generally lower than that of electrons, which is consistent with a valence band that is more dispersive than the conduction band. Apart from the effective mass, the carrier mobility is also strongly correlated with the elastic constant  $(C_{3D})$  and deformation potential  $(E_1)$ , as shown in eq 1.  $C_{3D}$  and  $E_1$  were then obtained with tensile and compression strains. The total energies and energy positions of the VBM and CBM relative to the vacuum as a function of strain are summarized in Figures S4 and S5. C<sub>3D</sub> was obtained by fitting the curve of total energy with strain, and  $E_1$  was calculated from the slope of the fitted lines of the VBM and CBM with strain. All of the  $C_{3D}$  and  $E_1$  values are summarized in Table 2. On the basis of the obtained effective mass,  $C_{3D}$ , and  $E_1$ , the carrier mobilities of the electron and hole are found to be hundreds of square centimeters per second per volt, except for the electron mobility of COF-COT-S-N (78.8 cm $^2$  s $^{-1}$  V $^{-1}$ ). The highest carrier mobility is

obtained in COF-COT-O-C, with values of 480 and 1418 cm² s<sup>-1</sup> V<sup>-1</sup> for the hole and electron, respectively. These values are comparable to those of inorganic semiconductors (e.g., SiC,  $^{30}$  400–900 cm² s<sup>-1</sup> V<sup>-1</sup> for the electron; CsPbI3,  $^{37}$  1399 cm² s<sup>-1</sup> V<sup>-1</sup> for the electron and 140 cm² s<sup>-1</sup> V<sup>-1</sup> for the hole; GaAs,  $^{31}$  3000 cm² s<sup>-1</sup> V<sup>-1</sup> for the electron) and T-carbon  $^{38}$  (2360 cm² s<sup>-1</sup> V<sup>-1</sup> for the electron and 270 cm² s<sup>-1</sup> V<sup>-1</sup> for the hole) and superior to the recorded mobility of 2D COFs (165 cm² s<sup>-1</sup> V<sup>-1</sup>).  $^{39}$ 

Because of the  $\pi$ – $\pi$ \* transition in the conjugated system, 3D FC-COFs are expected to exhibit good optical absorption at ultraviolet and visible light wavelengths. Next, we employ TDDFT with HSE06 to determine the optical properties, which are shown in Figure 4. The optical band gaps (the first bright exciton) for COF-COT-N-C, COF-COT-O-C, COF-COT-S-C, COF-COT-N-N, COF-COT-O-N, and COF-COT-S-N are 2.16, 1.73, 1.88, 2.66, 2.01, and 2.13 eV, respectively, demonstrating their ability to harvest broad visible light. The lower excitons are all bright, and the optical transitions associated with these excitons exhibit higher oscillator strengths, which are primarily due to the transition of electrons from the  $\pi$  to  $\pi^*$  orbitals. Therefore, these 3D FC-COFs exhibit broad and high absorption coefficients ( $\sim$ 2 × 10<sup>5</sup> cm<sup>-1</sup>) at visible light wavelengths. Additionally, the exciton binding energies  $(E_b)$  of the first bright exciton are approximately 15-25 meV and can spontaneously dissociate at room temperature, noting that the thermal fluctuation energy  $k_{\rm B}T$  at room temperature is ~25 meV.

Encouraged by the high optical absorbance and carrier mobility of all 3D FC-COFs, we further investigated their potential applications in photocatalytic water splitting. For the thermodynamic feasibility of overall photocatalytic water splitting, the energy positions of the CBM and VBM must straddle the redox potentials of water, meaning the energy position of CBM should be higher than the proton reduction potential ( $\rm H^+/H_{2}$ ,  $\rm -4.44~eV$ ) and the energy position of VBM

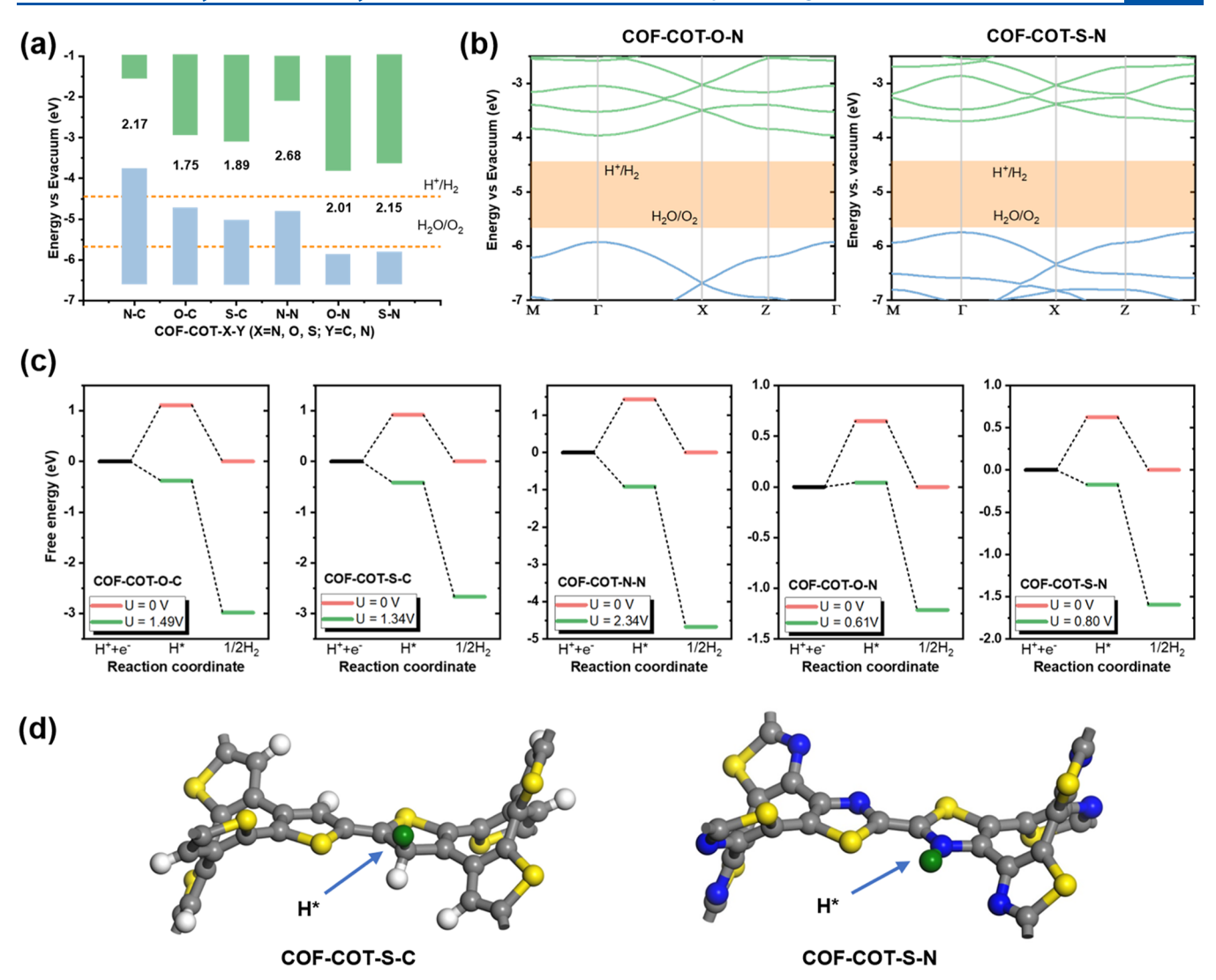


Figure 5. (a) Summary of the band alignment of 3D FC-COFs with respect to the vacuum level as well as the  $E_{\rm g}$  using the HSE06 method. The dashed orange lines are the proton reduction potential (H $^+$ /H $_2$ , -4.44 eV) and water oxidation potential (H $_2$ O/O $_2$ , -5.67 eV). (b) Band structures of COF-COT-O-N and COF-COT-S-N with high-symmetry k-points of M (0.5, 0.5, 0.5),  $\Gamma$  (0, 0, 0), X (0, 0.5, 0.5), and Z (0, 0, 0.5) relative to the vacuum level using the HSE06 method. (c) Free energy change involved in the hydrogen evolution reaction (HER) with and without an external potential. (d) Optimized structures of hydrogen absorption (H $^*$ ) on COF-COT-S-C and COF-COT-S-N. Gray, white, yellow, and blue spheres represent carbon, hydrogen, sulfur, and nitrogen atoms, respectively. H $^*$  is represented by green spheres.

should be lower than the water oxidation potential  $(H_2O/O_2)$ -5.67 eV). 43 To determine the energy levels of the VBM and CBM of 3D FC-COFs, we adopted the approach developed by Keith et al. for establishing the vacuum level of porous metalorganic frameworks.<sup>44</sup> In this method, a spherical average of the total electrostatic potential at the center of the pore, sampled with a radius of 2 Å, was utilized as the zero electrostatic potential to align the energy levels. This approach has demonstrated successful predictions of redox-active catalytic MOFs. Figure 5a summarizes the HSE06 band alignment of all 3D FC-COFs with respect to the vacuum level, with dashed orange lines representing redox potentials of water. Both COF-COT-O-N and COF-COT-S-N are found to be capable of overall water splitting, as confirmed by their HSE06-calculated band structures shown in Figure 5b. The CBMs of COF-COT-O-N and COF-COT-S-N are 0.61 and 0.80 eV higher, respectively, than the proton reduction potential (-4.44 eV), and their VBMs are 0.18 and 0.12 eV lower, respectively, than the water oxidation potential (-5.67)

eV). Except for overall water splitting, three other COFs (COF-COT-O-C, COF-COT-S-C, and COF-COT-N-N) are capable of the hydrogen evolution half-reaction with a hole sacrificial agent because their VBMs are higher than the water oxidation potential. Their CBMs are found to be 1.49, 1.34, and 2.34 eV higher, respectively, than the proton reduction potential. However, COF-COT-N-C cannot be used for water splitting due to its VBM and CBM being higher than the proton reduction potential.

Additionally, the photocatalytic reaction's feasibility and reaction rate also strongly depend on both the activity toward water splitting reactions of COFs and the redox ability of the photogenerated electrons and holes. Therefore, we investigated the hydrogen evolution reaction (HER) within the active sites on COFs using the computational hydrogen electrode model (see the computational details in Methods). In this model, the adsorption of hydrogen (H\*) serves as an important intermediate state of the HER, and the driving force of HER comes from the photogenerated electrons on the CBM, which

can be determined using the energy difference between the CBM and proton reduction potential.  $^{9,45}$  Figure 5c illustrates the calculated free energy changes of HER within COF-COT-O-C, COF-COT-S-C, COF-COT-N-N, COF-COT-O-N, and COF-COT-S-N. In the absence of photoexcitation (U = 0 V), the formation of H\* is exothermic with positive free energy changes of 1.11, 0.92, 1.42, 0.65, and 0.63 eV for COF-COT-O-C, COF-COT-S-C, COF-COT-N-N, COF-COT-O-N, and COF-COT-S-N, respectively. The formation of H\* and release of H<sub>2</sub> are thermodynamically unfavorable. However, upon light irradiation, the free energy changes of HER are all downhill with the corresponding external potential provided by photogenerated electrons, except for the case of COF-COT-O-N. Hence, COF-COT-O-C, COF-COT-S-C, COF-COT-N-N, and COF-COT-S-N can efficiently split water under acidic conditions upon light irradiation to produce hydrogen. For COF-COT-O-N, the free energy change when forming H\* is slightly positive (43 meV), which is close to the thermal fluctuation energy  $k_{\rm B}T$  at room temperature (25 meV). The active sites for HER are found on the Y atom sites, namely, the C and N atoms with sp<sup>2</sup> hybridization. The optimized structures of H\* are shown in Figure 5d and Figure S6. With regard to the oxygen evolution reaction (OER) on COF-COT-O-N and COF-COT-S-N, as the external potential provided by holes is relatively low (0.18 and 0.12 eV for COF-COT-O-N and COF-COT-S-N, respectively), the COFs are expected to produce O2 with the engineering of the OER cocatalysts.

In summary, we proposed six 3D FC-COFs (COF-COT-X-Y, where X = N, O, or S and Y = C or N) with a topological assembly of COT derivatives for photocatalytic water splitting. The structural, electronic, optical, and photocatalytic properties were studied on the basis of first-principles computations, from which the structural properties of 3D FC-COFs photocatalysts were established. We demonstrated that these 3D FC-COFs are semiconductors with outstanding optical absorption and carrier transport properties. The materials exhibit tunable direct band gaps ranging from 1.75 to 2.68 eV, with optical absorption coefficients of >2  $\times$  10<sup>5</sup> cm<sup>-1</sup> in the visible light range. The 3D FC-COFs show quasi-isotropic transport behavior, and their carrier mobility can reach 480 and 1400 cm<sup>2</sup> s<sup>-1</sup> V<sup>-1</sup> for holes and electrons, respectively, which are comparable to those of inorganic semiconductors and superior to those of 2D COFs with the recorded mobility. More importantly, two 3D FC-COFs have been identified to function as overall water splitting photocatalysts, and three other 3D FC-COFs can serve as hydrogen evolution halfreaction photocatalysts. This work paves the way for future applications of 3D FC-COFs in photocatalysis and optoelectronics.

# METHODS

All first-principles calculations based on density functional theory (DFT) were carried out using the Vienna Ab Initio Simulation Package (VASP) with the projector-augmented wave (PAW) method. Structural optimization was performed using the Perdew–Burke–Ernzerhof (PBE) exchange-correlation functional within the generalized gradient approximation (GGA). The weak van der Waals interaction was described with the DFT-D3 method with BJ damping. A Gamma-centered Monkhorst–Pack k-mesh was utilized for k-point sampling, with an interval of <0.03 Å<sup>-1</sup> for both structural optimization and self-consistent calculations. The

ENCUT was set to 500 eV, and the convergence thresholds for energy and force were 10<sup>-6</sup> eV and 0.01 eV/Å, respectively. The band gaps and band alignments were calculated using the screened hybrid functional HSE06.<sup>52</sup> The computational data postanalysis, COF structural analysis, and charge density visualization were performed using VASPKIT,<sup>53</sup> Zeo++,<sup>54</sup> and VESTA,<sup>55</sup> respectively.

The carrier mobility was determined using the deformation potential theory developed by Bardeen and Shockley.  $^{38,56}$  For 3D materials, the carrier mobility ( $\mu$ ) can be expressed using the effective mass approximation as follows:

$$\mu_{\rm 3D} = \frac{2\sqrt{2\pi}e\hbar^4 C_{\rm 3D}}{3(\kappa_{\rm B}T)^{3/2}m^{*5/2}E_{\rm 1}^2} \tag{1}$$

where  $k_{\rm B}$  represents Boltzmann's constant,  $\hbar$  is Planck's constant, and T is the temperature (300 K).  $C_{\rm 3D}$  denotes the 3D elastic constant, which is defined as  $C_{\rm 3D}=(\partial^2 E/\partial\delta^2)/V_0$ , where  $V_0$  is the equilibrium cell volume, E denotes the total energy, and  $\delta$  represents the applied strain.  $E_1$  is the deformation potential that is proportional to the VBM or CBM shift induced by the applied strain.  $E_1$  is expressed as  $\Delta E/(\Delta L/L_0)$ , where  $\Delta E$  denotes the energy change of the VBM or CBM as a function of lattice dilation with a step of 0.2%.  $m^*$  represents the effective mass in the transport direction and can be computed as  $m^* = \hbar^2 [\partial^2 E(k)/\partial k^2]^{-1}$ , where k denotes the wave-vector magnitude in momentum space. In this work, we calculated the effective masses using the HSE06 method while obtaining the deformation potentials and elastic constants with the PBE method.

To consider excitonic effects, we used time-dependent Hartree–Fock calculations on top of the HSE06 eigenenergies and eigenstates with the Casida equation to determine the optical properties. The Casida equation provided the exciton eigenenergies and oscillator strengths. The time-dependent Hartree–Fock method has been demonstrated to be reliable in describing the exciton absorption spectrum and offers significant computational advantages for large systems such as fullerene networks. The exciton binding energy  $(E_{\rm b})$  was calculated as the difference between the HSE06 eigenenergy and exciton eigenenergy. Optical absorption coefficients were obtained from the dielectric functions:

$$\alpha(\omega) = \sqrt{2}\,\omega[\sqrt{\varepsilon_1^{\,2}(\omega) + \varepsilon_2^{\,2}(\omega)} - \varepsilon_1(\omega)]^{1/2} \tag{2}$$

where  $\varepsilon_1(\omega)$  and  $\varepsilon_2(\omega)$  represent the imaginary and real parts of the dielectric functions, respectively.

The free energy change of hydrogen adsorption ( $\Delta G_{\mathrm{H}^*}$ ) was determined using a computational hydrogen electrode model developed by Nørskov et al. <sup>59-61</sup> The calculation was performed using the equation  $\Delta G_{\mathrm{H}^*} = \Delta E_{\mathrm{H}^*} + \Delta \mathrm{ZPE} - T\Delta S$ , where  $\Delta E_{\mathrm{H}^*}$  is the hydrogen chemisorption energy,  $\Delta \mathrm{ZPE}$  and  $\Delta S$  denote the zero-point energy and the entropy difference between the adsorbed hydrogen and its gas phase, respectively, and T is set to 298 K. The zero-point energy and entropy for the adsorbed hydrogen were calculated by a vibrational frequency calculation using density functional perturbation theory (DFPT). <sup>62</sup> The entropy of  $H_2$  was obtained from the Computational Chemistry Comparison and Benchmark Database (CCCBDB). <sup>63</sup>

#### ASSOCIATED CONTENT

# Supporting Information

The Supporting Information is available free of charge at https://pubs.acs.org/doi/10.1021/acs.jpclett.3c01850.

> Calculated phonon spectrum and first-principles molecular dynamics (MD) simulations, double and single bond lengths in 3D FC-COFs, summary of effective masses for electrons and holes, total energies, VBMs, and CBMs as a function of strain, and optimized structures of hydrogen absorption on COF-COT-O-C, COF-COT-N-N, and COF-COT-O-N (PDF)

## AUTHOR INFORMATION

## **Corresponding Authors**

Xu Zhang - Department of Physics and Astronomy, California State University Northridge, Northridge, California 91330-8268, United States; orcid.org/0000-0002-6491-3234; Email: xu.zhang@csun.edu

Yangyang Wan - Institute for Advanced Materials, School of Materials Science and Engineering, Jiangsu University, Zhenjiang, Jiangsu 212013, China; o orcid.org/0009-0001-0214-4046; Email: yangyang.wan@ujs.edu.cn

#### Authors

Pengting Sun - Institute for Advanced Materials, School of Materials Science and Engineering, Jiangsu University, Zhenjiang, Jiangsu 212013, China

Lebin Shi - Institute for Advanced Materials, School of Materials Science and Engineering, Jiangsu University, Zhenjiang, Jiangsu 212013, China

Xiaohong Yan - Institute for Advanced Materials, School of Materials Science and Engineering, Jiangsu University, Zhenjiang, Jiangsu 212013, China

Complete contact information is available at: https://pubs.acs.org/10.1021/acs.jpclett.3c01850

#### **Author Contributions**

Y.W. and X.Z. conceived and supervised the entire project. Y.W., P.S., and L.S. carried out first-principles computations. Y.W. and X.Z. wrote the manuscript and analyzed the data. All authors contributed to the discussion and revisions.

#### Notes

The authors declare no competing financial interest.

# ACKNOWLEDGMENTS

The work was supported by the National Natural Science Foundation of China (22209061), the U.S. National Science Foundation (Grants DMR-2105918 and DMR-1828019), and the Start-up Fund for Senior Talents in Jiangsu University (21JDG060). The theoretical calculations were supported by the Hefei advanced computing center.

# REFERENCES

- (1) Zhou, P.; Navid, I. A.; Ma, Y.; Xiao, Y.; Wang, P.; Ye, Z.; Zhou, B.; Sun, K.; Mi, Z. Solar-to-Hydrogen Efficiency of More Than 9% in Photocatalytic Water Splitting. Nature 2023, 613 (7942), 66-70.
- (2) Takata, T.; Jiang, J.; Sakata, Y.; Nakabayashi, M.; Shibata, N.; Nandal, V.; Seki, K.; Hisatomi, T.; Domen, K. Photocatalytic Water Splitting with a Quantum Efficiency of Almost Unity. Nature 2020, 581 (7809), 411–414.

(3) Tao, X.; Zhao, Y.; Wang, S.; Li, C.; Li, R. Recent Advances and Perspectives for Solar-Driven Water Splitting Using Particulate Photocatalysts. Chem. Soc. Rev. 2022, 51 (9), 3561-3608.

pubs.acs.org/JPCL

- (4) Lee, W. H.; Lee, C. W.; Cha, G. D.; Lee, B.-H.; Jeong, J. H.; Park, H.; Heo, J.; Bootharaju, M. S.; Sunwoo, S.-H.; Kim, J. H.; Ahn, K. H.; Kim, D.-H.; Hyeon, T. Floatable Photocatalytic Hydrogel Nanocomposites for Large-Scale Solar Hydrogen Production. Nat. Nanotechnol. 2023, 18, 754-762.
- (5) Liu, S.; Wang, M.; He, Y.; Cheng, Q.; Qian, T.; Yan, C. Covalent Organic Frameworks Towards Photocatalytic Applications: Design Principles, Achievements, and Opportunities. Coord. Chem. Rev. 2023, 475, No. 214882.
- (6) Qian, Z.; Wang, Z. J.; Zhang, K. A. Covalent Triazine Frameworks as Emerging Heterogeneous Photocatalysts. Chem. Mater. 2021, 33 (6), 1909-1926.
- (7) Fang, Y. X.; Hou, Y. D.; Fu, X. Z.; Wang, X. C. Semiconducting Polymers for Oxygen Evolution Reaction under Light Illumination. Chem. Rev. 2022, 122 (3), 4204-4256.
- (8) Yang, L.; Peng, Y.; Luo, X.; Dan, Y.; Ye, J.; Zhou, Y.; Zou, Z. Beyond  $C_3N_4$   $\pi$ -Conjugated Metal-Free Polymeric Semiconductors for Photocatalytic Chemical Transformations. Chem. Soc. Rev. 2021, 50 (3), 2147-2172.
- (9) Wan, Y.; Wang, L.; Xu, H.; Wu, X.; Yang, J. A Simple Molecular Design Strategy for Two-Dimensional Covalent Organic Framework Capable of Visible-Light-Driven Water Splitting. J. Am. Chem. Soc. **2020**, 142 (9), 4508–4516.
- (10) Banerjee, T.; Podjaski, F.; Kröger, J.; Biswal, B. P.; Lotsch, B. V. Polymer Photocatalysts for Solar-to-Chemical Energy Conversion. Nat. Rev. Mater. 2021, 6 (2), 168-190.
- (11) Zhang, W.; Chen, L.; Dai, S.; Zhao, C.; Ma, C.; Wei, L.; Zhu, M.; Chong, S. Y.; Yang, H.; Liu, L.; et al. Reconstructed Covalent Organic Frameworks. Nature 2022, 604 (7904), 72-79.
- (12) Jing, Y.; Zhu, X. Y.; Maier, S.; Heine, T. 2D Conjugated Polymers: Exploiting Topological Properties for the Rational Design of Metal-Free Photocatalysts. Trends. Chem. 2022, 4 (9), 792-806.
- (13) Jing, Y.; Zhou, Z.; Geng, W.; Zhu, X.; Heine, T. 2D Honeycomb-Kagome Polymer Tandem as Effective Metal-Free Photocatalysts for Water Splitting. Adv. Mater. 2021, 33 (21), No. 2008645.
- (14) Li, Y.; Song, X. Y.; Zhang, G.; Wang, L.; Liu, Y.; Chen, W. H.; Chen, L. 2D Covalent Organic Frameworks Toward Efficient Photocatalytic Hydrogen Evolution. ChemSusChem 2022, 15 (15), No. e202200901.
- (15) Wang, Y.; Zhao, Y.; Li, Z. 2D Covalent Organic Frameworks as Photocatalysts for Solar Energy Utilization. Macromol. Rapid Commun. 2022, 43 (16), No. 2200108.
- (16) Wang, Y.; Hao, W.; Liu, H.; Chen, R.; Pan, Q.; Li, Z.; Zhao, Y. Facile Construction of Fully sp<sup>2</sup>-Carbon Conjugated Two-Dimensional Covalent Organic Frameworks Containing Benzobisthiazole Units. Nat. Commun. 2022, 13 (1), 100.
- (17) Yu, H.; Wang, D. Suppressing the Excitonic Effect in Covalent Organic Frameworks for Metal-Free Hydrogen Generation. JACS Au 2022, 2 (8), 1848-1856.
- (18) Yang, Y.; Chu, X.; Zhang, H.-Y.; Zhang, R.; Liu, Y.-H.; Zhang, F.-M.; Lu, M.; Yang, Z.-D.; Lan, Y.-Q. Engineering  $\beta$ -Ketoamine Covalent Organic Frameworks for Photocatalytic Overall Water Splitting. Nat. Commun. 2023, 14 (1), 593.
- (19) Gao, P.; Zhang, L.; Fu, C.; Tian, Y.; Li, X.; Li, X.; Yang, J. Promoting Water Activation by Photogenerated Holes in Monolayer C<sub>2</sub>N. J. Phys. Chem. Lett. **2022**, 13 (15), 3332-3337.
- (20) Fu, C.-F.; Zhao, C.; Zheng, Q.; Li, X.; Zhao, J.; Yang, J. Halogen Modified Two-Dimensional Covalent Triazine Frameworks as Visible-Light Driven Photocatalysts for Overall Water Splitting. Sci. China. Chem. 2020, 63 (8), 1134-1141.
- (21) Wu, M.; Shan, Z.; Wang, J.; Liu, T.; Zhang, G. Three-Dimensional Covalent Organic Framework with tty Topology for Enhanced Photocatalytic Hydrogen Peroxide Production. Chem. Eng. J. 2023, 454, No. 140121.

- (22) Ding, J.; Guan, X.; Lv, J.; Chen, X.; Zhang, Y.; Li, H.; Zhang, D.; Qiu, S.; Jiang, H.-L.; Fang, Q. Three-Dimensional Covalent Organic Frameworks with Ultra-Large Pores for Highly Efficient Photocatalysis. *J. Am. Chem. Soc.* **2023**, *145* (5), 3248–3254.
- (23) Ma, S.; Deng, T.; Li, Z.; Zhang, Z.; Jia, J.; Li, Q.; Wu, G.; Xia, H.; Yang, S.-W.; Liu, X. Photocatalytic Hydrogen Production on a sp<sup>2</sup>-Carbon-Linked Covalent Organic Framework. *Angew. Chem., Int. Ed.* **2022**, *61* (42), No. e202208919.
- (24) Li, Y.; Yang, L.; He, H.; Sun, L.; Wang, H.; Fang, X.; Zhao, Y.; Zheng, D.; Qi, Y.; Li, Z.; Deng, W. In Situ Photodeposition of Platinum Clusters on a Covalent Organic Framework for Photocatalytic Hydrogen Production. *Nat. Commun.* **2022**, *13* (1), 1355.
- (25) Guan, X.; Chen, F.; Qiu, S.; Fang, Q. Three-Dimensional Covalent Organic Frameworks: From Synthesis to Applications. *Angew. Chem., Int. Ed.* **2023**, 62 (3), No. e202213203.
- (26) Wang, Y.; Zhang, Y.; Wang, S.; Cao, D. Saddle-Shaped Building Blocks: A New Concept for Designing Fully Conjugated 3D Organic Semiconducting Materials. *Chem. Eur. J.* **2021**, 27 (47), 12012–12018.
- (27) Jin, E.; Geng, K.; Fu, S.; Yang, S.; Kanlayakan, N.; Addicoat, M. A.; Kungwan, N.; Geurs, J.; Xu, H.; Bonn, M.; et al. Exceptional Electron Conduction in Two-Dimensional Covalent Organic Frameworks. *Chem* **2021**, *7* (12), 3309–3324.
- (28) Wang, M.; Wang, M.; Lin, H.-H.; Ballabio, M.; Zhong, H.; Bonn, M.; Zhou, S.; Heine, T.; Cánovas, E.; Dong, R.; Feng, X. High-Mobility Semiconducting Two-Dimensional Conjugated Covalent Organic Frameworks with p-Type Doping. *J. Am. Chem. Soc.* **2020**, 142 (52), 21622–21627.
- (29) Jin, E.; Fu, S.; Hanayama, H.; Addicoat, M. A.; Wei, W.; Chen, Q.; Graf, R.; Landfester, K.; Bonn, M.; Zhang, K. A.; et al. A Nanographene-Based Two-Dimensional Covalent Organic Framework as a Stable and Efficient Photocatalyst. *Angew. Chem., Int. Ed.* **2022**, *61* (5), No. e202114059.
- (30) Roschke, M.; Schwierz, F. Electron Mobility Models for 4H, 6H, and 3C SiC [MESFETs]. *IEEE Trans. Electron Devices* **2001**, 48 (7), 1442–1447.
- (31) Balaghi, L.; Shan, S.; Fotev, I.; Moebus, F.; Rana, R.; Venanzi, T.; Hübner, R.; Mikolajick, T.; Schneider, H.; Helm, M.; Pashkin, A.; Dimakis, E. High Electron Mobility in Strained GaAs Nanowires. *Nat. Commun.* **2021**, *12* (1), 6642.
- (32) Bao, R.; Xiang, Z.; Qiao, Z.; Yang, Y.; Zhang, Y.; Cao, D.; Wang, S. Designing Thiophene-Enriched Fully Conjugated 3D Covalent Organic Framework as Metal-Free Oxygen Reduction Catalyst for Hydrogen Fuel Cells. *Angew. Chem., Int. Ed.* 2023, 62 (4), No. e202216751.
- (33) Wang, S.; Da, L.; Hao, J.; Li, J.; Wang, M.; Huang, Y.; Li, Z.; Liu, Z.; Cao, D. A Fully Conjugated 3D Covalent Organic Framework Exhibiting Band-Like Transport with Ultrahigh Electron Mobility. *Angew. Chem., Int. Ed.* **2021**, *60* (17), 9321–9325.
- (34) Wu, M.; Shan, Z.; Wang, J.; Gu, Z.; Wu, X.; Xu, B.; Zhang, G. Three-Dimensional Covalent Organic Frameworks Based on a  $\pi$ -Conjugated Tetrahedral Node. *Chem. Commun.* **2021**, *57* (80), 10379–10382.
- (35) Wang, S.; Li, X. X.; Da, L.; Wang, Y.; Xiang, Z.; Wang, W.; Zhang, Y. B.; Cao, D. A Three-Dimensional sp<sup>2</sup> Carbon-Conjugated Covalent Organic Framework. *J. Am. Chem. Soc.* **2021**, *143* (38), 15562–15566.
- (36) Ghosh, S.; Nakada, A.; Springer, M. A.; Kawaguchi, T.; Suzuki, K.; Kaji, H.; Baburin, I.; Kuc, A.; Heine, T.; Suzuki, H.; Abe, R.; Seki, S. Identification of Prime Factors to Maximize the Photocatalytic Hydrogen Evolution of Covalent Organic Frameworks. *J. Am. Chem. Soc.* 2020, 142 (21), 9752–9762.
- (37) Gao, L. K.; Tang, Y. L. Theoretical Study on the Carrier Mobility and Optical Properties of  $CsPbI_3$  by DFT. *ACS Omega* **2021**, 6 (17), 11545–11555.
- (38) Sun, P.-P.; Bai, L.; Kripalani, D. R.; Zhou, K. A New Carbon Phase with Direct Bandgap and High Carrier Mobility as Electron Transport Material for Perovskite Solar Cells. *npj Comput. Mater.* **2019**, *5* (1), 9.

- (39) Fu, S.; Jin, E.; Hanayama, H.; Zheng, W.; Zhang, H.; Di Virgilio, L.; Addicoat, M. A.; Mezger, M.; Narita, A.; Bonn, M.; Mullen, K.; Wang, H. I. Outstanding Charge Mobility by Band Transport in Two-Dimensional Semiconducting Covalent Organic Frameworks. J. Am. Chem. Soc. 2022, 144 (16), 7489–7496.
- (40) Fukuzumi, K.; Nishii, Y.; Miura, M. Palladium-Catalyzed Synthesis of Heteroarene-Fused Cyclooctatetraenes through Dehydrogenative Cyclodimerization. *Angew. Chem., Int. Ed.* **2017**, *56* (41), 12746–12750.
- (41) Sheng, X. L.; Yan, Q. B.; Ye, F.; Zheng, Q. R.; Su, G. T-Carbon: a Novel Carbon Allotrope. *Phys. Rev. Lett.* **2011**, *106* (15), No. 155703.
- (42) Steinmann, S. N.; Mo, Y.; Corminboeuf, C. How do Electron Localization Functions Describe  $\pi$ -Electron Delocalization? *Phys. Chem. Chem. Phys.* **2011**, *13* (46), 20584–20592.
- (43) Samanta, B.; Morales-García, Á.; Illas, F.; Goga, N.; Anta, J. A.; Calero, S.; Bieberle-Hütter, A.; Libisch, F.; Muñoz-García, A. B.; Pavone, M.; Caspary Toroker, M. Challenges of Modeling Nanostructured Materials for Photocatalytic Water Splitting. *Chem. Soc. Rev.* 2022, *51* (9), 3794–3818.
- (44) Butler, K. T.; Hendon, C. H.; Walsh, A. Electronic Chemical Potentials of Porous Metal-Organic Frameworks. *J. Am. Chem. Soc.* **2014**, *136* (7), 2703–2706.
- (45) Peng, B. Monolayer Fullerene Networks as Photocatalysts for Overall Water Splitting. *J. Am. Chem. Soc.* **2022**, *144* (43), 19921–19931.
- (46) Kresse, G.; Hafner, J. Ab Initio Molecular-Dynamics Simulation of the Liquid-Metal-Amorphous-Semiconductor Transition in Germanium. *Phys. Rev. B* **1994**, *49* (20), 14251–14269.
- (47) Kresse, G.; Furthmuller, J. Efficient Iterative Schemes for Ab Initio Total-Energy Calculations Using a Plane-Wave Basis Set. *Phys. Rev. B* **1996**, *54* (16), 11169.
- (48) Kresse, G.; Furthmüller, J. Efficiency of Ab-Initio Total Energy Calculations for Metals and Semiconductors Using a Plane-Wave Basis Set. *Comput. Mater. Sci.* **1996**, *6* (1), 15–50.
- (49) Kresse, G.; Joubert, D. From Ultrasoft Pseudopotentials to the Projector Augmented-Wave Method. *Phys. Rev. B* **1999**, *59* (3), 1758–1775.
- (50) Perdew, J. P.; Burke, K.; Ernzerhof, M. Generalized Gradient Approximation Made Simple. *Phys. Rev. Lett.* **1996**, 77 (18), 3865–3868.
- (51) Grimme, S.; Antony, J.; Ehrlich, S.; Krieg, H. A Consistent and Accurate Ab Initio Parametrization of Density Functional Dispersion Correction (DFT-D) for the 94 Elements H-Pu. *J. Chem. Phys.* **2010**, 132 (15), No. 154104.
- (52) Heyd, J.; Scuseria, G. E.; Ernzerhof, M. Hybrid Functionals Based on a Screened Coulomb Potential. *J. Chem. Phys.* **2003**, *118* (18), 8207–8215.
- (53) Wang, V.; Xu, N.; Liu, J. C.; Tang, G.; Geng, W. VASPKIT: A User-Friendly Interface Facilitating High-Throughput Computing and Analysis Using VASP Code. *Comput. Phys. Commun.* **2021**, 267, No. 108033.
- (54) Willems, T. F.; Rycroft, C. H.; Kazi, M.; Meza, J. C.; Haranczyk, M. Algorithms and Tools for High-Throughput Geometry-Based Analysis of Crystalline Porous Materials. *Microporous Mesoporous Mater.* **2012**, *149* (1), 134–141.
- (55) Momma, K.; Izumi, F. VESTA3 for Three-Dimensional Visualization of Crystal, Volumetric and Morphology Data. *J. Appl. Crystallogr.* **2011**, *44* (6), 1272–1276.
- (56) Bardeen, J.; Shockley, W. Deformation Potentials and Mobilities in Non-Polar Crystals. *Phys. Rev. Appl.* **1950**, 80 (1), 72–80.
- (57) Sander, T.; Kresse, G. Macroscopic Dielectric Function within Time-Dependent Density Functional Theory-Real Time Evolution versus The Casida Approach. *J. Chem. Phys.* **2017**, *146* (6), No. 064110.
- (58) Peng, B.; Zhang, H.; Shao, H.; Xu, K.; Ni, G.; Wu, L.; Li, J.; Lu, H.; Jin, Q.; Zhu, H. Room-Temperature Bound Exciton with Long

Lifetime in Monolayer GaN. ACS Photonics 2018, 5 (10), 4081–4088.

- (59) Skulason, E.; Karlberg, G. S.; Rossmeisl, J.; Bligaard, T.; Greeley, J.; Jonsson, H.; Norskov, J. K. Density Functional Theory Calculations for the Hydrogen Evolution Reaction in an Electrochemical Double Layer on the Pt(111) Electrode. *Phys. Chem. Chem. Phys.* **2007**, 9 (25), 3241–3250.
- (60) Nørskov, J. K.; Bligaard, T.; Logadottir, A.; Kitchin, J. R.; Chen, J. G.; Pandelov, S.; Stimming, U. Trends in the Exchange Current for Hydrogen Evolution. *J. Electrochem. Soc.* **2005**, *152* (3), J23–J26.
- (61) Nørskov, J. K.; Rossmeisl, J.; Logadottir, A.; Lindqvist, L.; Kitchin, J. R.; Bligaard, T.; Jónsson, H. Origin of the Overpotential for Oxygen Reduction at a Fuel-Cell Cathode. *J. Phys. Chem. B* **2004**, *108* (46), 17886–17892.
- (62) Baroni, S.; Giannozzi, P.; Isaev, E. Density-Functional Perturbation Theory for Quasi-Harmonic Calculations. *Rev. Mineral. Geochem.* **2010**, *71* (1), 39–57.
- (63) Johnson, R. D. NIST Computational Chemistry Comparison and Benchmark Database, NIST Standard Reference Database Number 101 Release 22, May 2022. http://cccbdb.nist.gov/.

# ☐ Recommended by ACS

## A Data-Driven Search of Two-Dimensional Covalent Organic Frameworks for Visible-Light-Driven Overall Water Splitting

Yangyang Wan, Xiaojun Wu, et al.

AUGUST 14, 2023

THE JOURNAL OF PHYSICAL CHEMISTRY LETTERS

READ 🗹

# Saturated Linkers in Two-Dimensional Covalent Organic Frameworks Boost Their Luminescence

Meijia Yang, Klaus Müllen, et al.

JUNE 20, 2023

JOURNAL OF THE AMERICAN CHEMICAL SOCIETY

READ 🗹

# Postsynthetic Annulation of Three-Dimensional Covalent Organic Frameworks for Boosting CO<sub>2</sub> Photoreduction

Pengfei Dong, Jianping Lei, et al.

JULY 08, 2023

JOURNAL OF THE AMERICAN CHEMICAL SOCIETY

READ 🗹

# Dithiophenedione-Based Covalent Organic Frameworks for Supercapacitive Energy Storage

Shuang Li, Pradip Pachfule, et al.

SEPTEMBER 14, 2023

ACS APPLIED ENERGY MATERIALS

READ 🗹

Get More Suggestions >